Journal of Materials Chemistry A

Accepted Manuscript

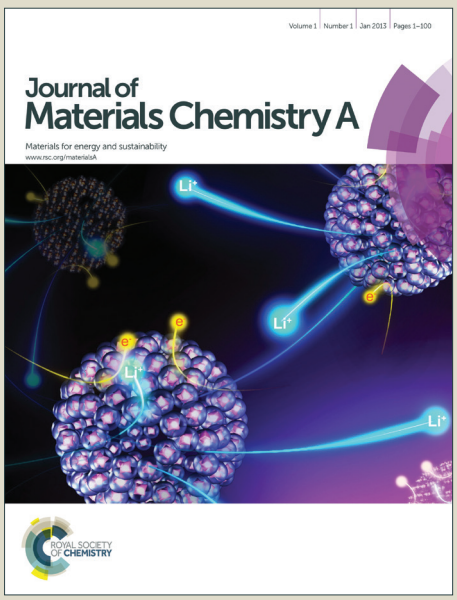

ROYAL SOCIETY OF CHEMISTRY

www.rsc.org/materialsA

Three-dimensional honeycomb-like hierarchical structured carbon for High-performance supercapacitors derived from high-ash-content sewage sludge

Haobin Feng, Mingtao Zheng,* Hanwu Dong, Yong Xiao, Hang Hu, Zhongxin Sun, Chao Long, Yijin Cai, Xiao Zhao, Haoran Zhang, Bingfu Lei and Yingliang Liu*

Three-dimensional honeycomb-like hierarchical structured carbon was synthesized from high-ash-content sewage sludge and exhibited remarkable specific capacitance and excellent long-term cycling stability for high-performance supercapacitors.

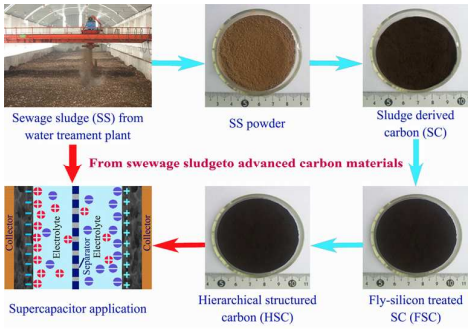

Journal of Materials Chemistry A

ARTICLE

Three-dimensional honeycomb-like hierarchical structured carbon for high-performance supercapacitors derived from high-ash-content sewage sludge

Received 00th January 20xx,
Accepted 00th January 20xx

DOI: 10.1039/x0xx00000x

www.rsc.org/

Haobin Feng,[a] Mingtao Zheng,*[a,b] Hanwu Dong,[a] Yong Xiao,[b] Hang Hu,[a] Zhongxin Sun,[a] Chao Long,[a] Yijin Cai,[a] Xiao Zhao,[a] Haoran Zhang,[b] Bingfu Lei[a,b] and Yingliang Liu *[a,b]

In this work we demonstrate that three-dimensional honeycomb-like hierarchical structured carbon (HSC) can be prepared by using high-ash-content sewage sludge as carbon precursor for the first time. The fly-silicon process acts a crucial role in the formation of honeycomb-like hierachical structures. The as-resulted HSC exhibits novel honeycomb-like framework, high specific surface area (2839 m^2 g^{-1}), large pore volume (2.65 cm^3 g^{-1}), interconnected hierarchical porosity, and excellent electrochemical performance. The high specific capacitance of 379 F g^{-1} as well as excellent rate capability and outstanding cycling stability (over 90% capacitance retention after 20,000 cycles even at a high current density of 20 A g^{-1}), makes it suitable for high-performance supercapacitor electrode materials. The assembled HSC//HSC symmetric supercapacitor presents an enhanced supercapacitive behavior with high energy density of 30.5 Wh kg^{-1} in aqueous solution. The strategy provides an effective method to achieve high-performance electrode materials derived from other high-ash-content biomass wastes for supercapacitors.

Introduction

Sewage sludge (SS) is a major by-product generated from wastewater treatment plants, and it is predicted to increase stably every year due to the rapid growth of population, urbanization, and industrialization. Nowadays, the management of SS has become a seriously environmental problem in large cities all over the world. Various strategies, such as landfilling, composting, thermal treatment, and land application following anaerobic and aerobic digestion, have been employed to treat waste sludge for many years, but each of these methods encounters its own hindrances.[1,2] For example, land application is hindered by the land retention capacity, and certain risks may also be caused by pathogens and heavy metals in the SS.[3] Nevertheless, it has been demonstrated that there were a large amount of microorganisms and complex organic matters including peptidoglycan, teichoic acids, and complex polysaccharides. Considering the huge amount and abundant organic components, it is highly feasible to convert such waste sludge into high value-added carbonaceous materials for applications in the field of energy storage and conversion.[4,5]

The ever-increasing needs for renewable energy and growing concerns of environmental protection have stimulated extensive investigation to develop efficient energy conversion and storage devices.[6-8] Supercapacitors, also known as electrochemical capacitors, have emerged as a promising candidate for energy storage over the past decade due to their merits of high power density, long cycling life, simple principle, and speedy dynamic of charge propagation.[9,10] Nanostructured electrode materials have been demonstrated superior electrochemical properties in producing high-performance supercapacitors.[11] Among various supercapacitor electrode materials, carbon-based materials are dominant for commercial supercapacitors owing to their high electrical conductivity, low cost and long cycling life.[12] Carbon materials with high surface area as well as a range of shapes, sizes and pore size distributions are being constantly developed and investigated as for potential supercapacitor electrodes.[13,14] To date, a lot of efforts have been devoted to the synthesis of novel carbon materials with diverse nanostructures including activated carbons,[15] nanotubes,[16] nanofibers,[17] templated porous carbons,[18] carbide-derived carbons,[19] graphene,[20] and their composites,[21] for supercapacitor application. However, these carbon-based supercapacitors have low capacitance and energy density, which severely limits their practical applications as high-performance energy storage devices due to their energy storage mechanism that is a purely physical process.[22]

To meet the continuously growing demands for high-efficiency energy storage devices in the modern society, it is urgent and significant to develop new carbon materials with favourable features such as high specific surface area, high

[a] Department of Materials Science and Engineering, College of Materials and Energy, South China Agricultural University, Guangzhou 510642, china. E-mail: mtzheng@scau.edu.cn (M. Zheng), tliuyl@163.com (Y. Liu); Tel/Fax: +86 20 8528 0319.
[b] Guangdong Provincial Engineering Technology Research Center for Optical Agriculture, Guangzhou 510642, China.

† Electronic Supplementary Information (ESI) available: Proximate and ultimate analyses and XRD pattern of SS, pore characteristics, SEM image of ASC, Bode plot, comparison of capacitive property, etc. See DOI: 10.1039/x0xx00000x

electrical conductivity, tuneable pore structure, and a stable three-dimensional (3D) hierarchical nanoarchitecture.[23] Recent studies have shown that 3D hierarchical nanostructures were a promising candidate for supercapacitors because these nanoarchitectures can provide continuous electron pathways to ensure good electrical contact and offer shortened diffusion pathways to facilitate ion transport.[24,25] For example, 3D graphene-based electrodes,[26,27] hierarchical porous carbons,[28] and hierarchical hybrid nanostructures,[29] have been developed. Despite these achievements, it is highly desirable to develop simple and scalable methods to synthesize 3D carbon nanostructures with high capacitance and excellent cycling stability for supercapacitors.

Recently, waste-biomass-derived carbons for the energy applications have received considerable attention owing to the growing scarcity of fossil energy.[30,31] However, the biomass-derived carbons for the supercapacitor electrode applications were primarily derived from lignocellulose biomass, such as wood and agriculture wastes.[32] More recently, the synthesis and supercapacitor application of sludge-derived carbons began to arouse researchers' interest.[33,34] For instance, Wang and co-workers prepared activated carbons with high electrochemical performance by using high-carbon-content pulp sludge generated in paper industry.[33] N-doped porous carbons with specific surface area of 940 m^2 g^{-1} and specific capacitance of 247 F g^{-1} in aqueous electrolyte have been prepared by pyrolysis of surplus sludge (a low ash content sludge).[34] However, to the best of our knowledge, there are no efforts devoted to the utilization of SS as precursor for preparing carbon-based electrode materials for supercapacitors because of its high ash content which is difficult to be removed effectively.

In this work, we demonstrate the synthesis of honeycomb-like hierarchical structured carbon (HSC) by using SS with high ash content as carbon precursor for the first time. The fly-silicon process was introduced to remove the ash content, which plays a crucial role in the formation of honeycomb-like HSC. The as-obtained HSC exhibits high specific surface area (2839 m^2 g^{-1}) and large pore volume (2.65 cm^3 g^{-1}). Furthermore, it combines hierarchical macro/nanostructures, namely, honeycomb-like morphology composed of nanosheets, macroporous frameworks, mesoporous walls, and microporous textures, which are favourable for diffusion of the active ions.[35] Benefiting from the unique 3D hierarchical nanostructures, the HSC presents high specific capacitance, excellent rate performance and long-term stability in aqueous electrolytes as electrode materials for high-performance supercapacitors.

Experimental section

Materials

The SS powder was collected from Liede Sewage Treatment Plant, Guangzhou, China. All chemical reagents were analytical grade and used as received without further purification. Ethanol, hydrofluoric acid, hydrochloric acid (HCl), nitric acid, sulfuric acid, and potassium hydroxide (KOH) was purchased from Guangzhou Chemical Reagent Factory.

Preparation of honeycomb-like hierarchical structured carbon (HSC) derived from sewage sludge

In a typical process, 20 g of SS was ground in an agate mortar into fine powder. The SS powder was put in a tube furnace under nitrogen (N_2, 99.99%) flow and carbonized at 700 °C for 3 h. Subsequently, the obtained sample (sludge-derived carbon, named as SC) was impregnated into 30 % hydrofluoric acid solution at the solid-liquid ratio of 1:1.2 (v/v), and then was evaporated at 120 °C. This process is called fly-silicon treatment. The resulted powder was washed with distilled water until the pH came near 7 and then dried at 80 °C for 12 h, and black fly-silicon-treated sludge-derived carbon (FSC) was obtained. The as-resulted FSC was then mixed with KOH at a KOH/C of x: 1 (x=1, 2，3 and 4) and activated in a fixed-bed reactor at a heating rate of 10 °C /min from room temperature to the 700 °C under a nitrogen (N_2, 99.99%) atmosphere (flow rate of 20 mL/min), and held at this temperature for 3 h. The product was washed with 3 M HCl aqueous solution, and then rinsed with deionized water and ethanol for several times. Finally, the product was dried at 80 °C for 12 h, and 3D honeycomb-like hierarchical structured carbon (HSC) was obtained. The samples activated by KOH with different KOH/C ratios of 1, 2, 3, and 4, were labeled as HSC-1, HSC-2, HSC-3, and HSC-4, respectively.

Morphology and structure characterization

The proximate analysis of SS powder was conducted according to ASTM E1755-01, ASTM E871-82 and ASTM E872-82 standards and the results were expressed in terms of moisture, ash, volatile matter. The activated carbons were analyzed for carbon, nitrogen, hydrogen, and oxygen (by difference) abundances using an EA2400 II elemental analyzer. The content of Si was measured by X-ray fluorescence (JSX-3400R, JEOL). Porous structure characteristics of the samples was determined from N_2 adsorption and desorption isotherms that were measured at 77 K using an automatic volumetric sorption analyzer (ASAP 2020, Micromeritics Instrument Corp.). The morphology was observed by the field emission scanning electron microscope (FESEM, ZEISS Ultra 55), transmission electron microscope (TEM, TECNAI 10), and high-resolution TEM (HRTEM, JEM2100HR). X-ray diffraction (XRD) patterns were obtained from an X-ray powder diffractometer (XD-2X/M4600, Cu Kα, λ = 1.54051 Å).

Electrochemical performance of HSC

The working electrode was prepared by mixing the as-prepared HSC, carbon black, and PTFE binder with a mass ratio of 80:10:10 in ethanol to obtain a paste, which was then dispersed on a nickel foam (current collector) as a 1 cm ×1 cm sheet before being pressed together, followed by drying at 105 °C overnight. The amount of active material loaded on the electrode is about 4.0 mg for each working electrode. In a three-electrode cell, the above loaded nickel foam, a Pt wire, and an Hg/HgO electrode were used as the working, counter, and reference electrodes, respectively. Cyclic voltammetry (CV) and galvanostatic charge/discharge (GCD) were conducted on a CHI660e electrochemical workstation (CHI Instruments Co.) at room temperature. Electrochemical impedance spectroscopy (EIS)

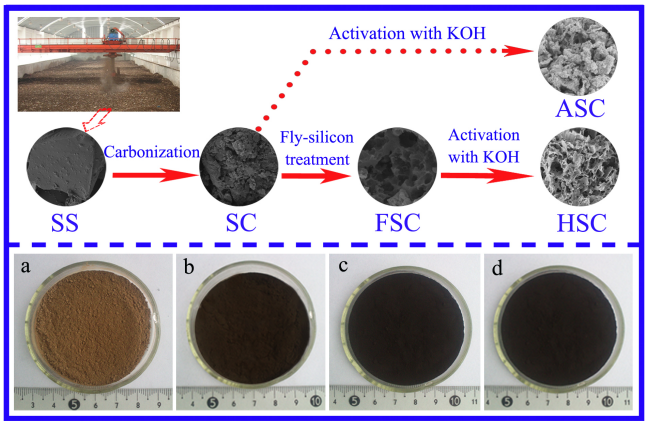

Fig. 1 (Up) Schematic of the synthesis process of 3D honeycomb-like hierarchical-structured carbon (HSC, with fly-silicon treatment) materials and activated sludge-derived carbon (ASC, without fly-silicon treatment). (Down) Photos of (a) sewage sludge (SS), (b) sludge-derived carbon (SC), (c) fly-silicon treatment SC (FSC), and (d) the as-obtained HSC materials by fly-silicon treatment and activation with KOH.

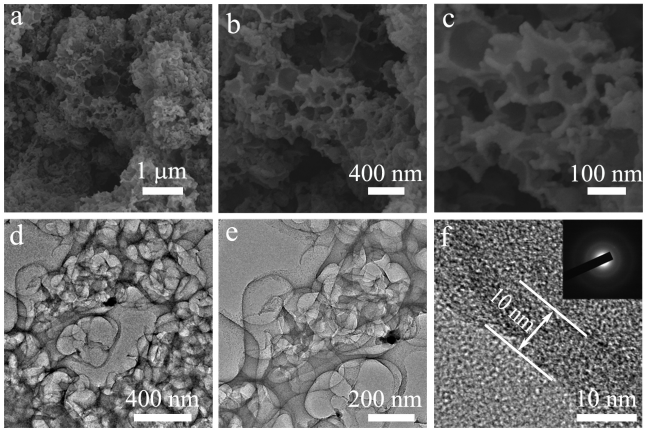

Fig. 2 FESEM images with different magnification (a-c), TEM images (d,e), and HRTEM image (f) of the unique i honeycomb-like HSC. Inset in (f) is the corresponding selected area electron diffraction pattern.

was performed on an Im6ex (Zahnex Corp.) electrochemical workstation. The frequency range of 100 kHz to 10 mHz at open circuit voltage. As for the assembly of symmetric supercapacitor, two electrodes with same size and HSC-3 active material loading (4.0 mg) were assembled with a glassy fibrous separator. The electrochemical measurements were measured in 1 M Na_2SO_4 aqueous electrolyte.

The complex capacitance was calculated from the EIS data according to the following equations[36,37]:

$$C^* = C' - iC'' \quad (1)$$

$$C' = Z''/\omega|Z|^2 \quad (2)$$

$$C'' = Z'/\omega|Z|^2 \quad (3)$$

where $\omega = 2\pi f$, f is the frequency. The relaxation time is defined as the reciprocal of relaxation frequencies corresponding to the maxima of C''.

The gravimetric specific capacitance of the electrodes can be calculated from the charge/discharge curves and CV test according to the following equations:

$$C_s = \frac{I\Delta t}{m\Delta V} \quad (4)$$

$$C_{CV} = \frac{\int Idu}{2vm\Delta V} \quad (5)$$

where C_s is the specific capacitance of the electrode materials calculated from GCD test, I is the constant current, m is the active mass, Δt is the discharge time, and ΔV is the discharge voltage excluding the IR drop. C_{cv} is the specific capacitance calculated from CV test, I is the constant current, m is the mass of that active materials, v is the scan rate, and ΔV is the potential range.

The area-normalized capacitance of the electrodes can be calculated from the charge/discharge curves and CV test according to the following equations:

$$C_{c,s} = C_s\rho \quad (6)$$

$$C_{c,CV} = C_{CV}\rho \quad (7)$$

where $C_{c,s}$ and $C_{c,CV}$ is the specific capacitance of the electrode materials calculated from the GCD and CV test respectively, and ρ is the weight of active material of per square centimetre.

The energy density (E) and power density (P) of the cell in the two-electrode configuration were calculated by using the following equations:

$$E = \frac{1}{2}CV^2 \quad (8)$$

$$P = \frac{E}{\Delta t} \quad (9)$$

where C represents the specific capacitance of supercapacitor, V refers to the potential change within the discharge time Δt.

Results and discussion

Fig. 1 illustrates the strategy for the synthesis of the HSC derived from high-ash-content SS and activated sludge-derived carbons (ASC) without fly-silicon treatment. The analysis of the composition of the employed SS powder (Table S1, see ESI) reveals a 69.33 % of ash, 2.39 % of moisture, and 24.48 % of Si content, indicating the high ash content of SS. The main crystalline phase of SS can be identified as SiO_2 (quartz, PDF no. 89-8937) from the XRD pattern (Fig. S1). SEM image shows that the SS powder consists of micro particles with sizes of 40-50 μm, and a large number of macropores can also be observed on the surface (Fig. S2a). After carbonized at high temperature, the yellowish-brown SS powder (Fig. 1a), was broken into finer particles with average size of about 12 μm (Fig. S2b), and brownish-black powder (SC) could be obtained (Fig. 1b). The main crystalline phase of SC was identified as the same quartz SiO_2 as in SS (Fig. S1). To remove the inorganic ash component (i.e. SiO_2), the resultant SC was treated by fly-silicon with hydrofluoric acid, and black FSC powder could be obtained (Fig. 1c). The ash content of FSC was reduced to 9.24 %, and the carbon content was increased from 11.59 to 50.61 % (Table S1). These results indicate that inorganic components can be removed effectively by this fly-silicon treatment, and the as-obtained FSC is mainly composed

of amorphous carbons (Fig. S1). On the other hand, the specific surface area of the as-resulted FSC is about 111 m^2 g^{-1}, which is three times larger than that of SC (Table S2). The as-resulted FSC was then mixed with KOH with various KOH/C mass ratios and further activated at 700 °C for 3 h, and finally 3D honeycomb-like HSC was obtained after HCl washing (Fig. 1d). The ash content of HSC was further reduced to 0.32 % and Si could not be detected. In comparison with HSC, ASC was prepared from activation of SC without fly-silicon treatment.

The morphology and microstructures of the resultant HSC-3 were characterized by FESEM and TEM. As showed in Fig. 2a, the as-prepared HSC-3 exhibits a 3D honeycomb-like hierarchical structure. The magnified FESEM image (Fig. 2b) shows an interconnected network of macropores with sizes ranging from 80 to 300 nm. These macropores networks will facilitate the diffusion process of electrolyte ions into the inner micropores at higher charging rates. It can be seen from Fig. 2c that the honeycomb-like hierarchical structures are composed of interconnected free-standing nanosheets. The mesopores with size of 5-10 nm and crimp for the outer edges of the nanosheets of the 3D interconnected porous network can also be observed. TEM image shown in Fig. 2d further confirms the interconnected hierarchical structures. The macropores and mesopores overlap each other to form the interconnected hierarchical pores (Fig. 2e). HRTEM image reveals the amorphous nature of HSC-3 (Fig. 2f). The thickness of the nanosheets of HSC-3 is about 10 nm. The corresponding selected area electron diffraction pattern (SAED, Fig. 2f inset) further illustrates the amorphous or disordered structural characteristic since only diffused rings can be observed, which is well consistent to the HRTEM results.

It is worth noting that only granular nanoparticles (ASC) were obtained without the fly-silicon treatment before KOH activation (Fig. S2d). It can also be seen that there was no honeycomb-like structure in the products, when hydrofluoric acid in the fly-silicon process was replaced by other acids such as hydrochloric, nitric, and sulfuric acid (Fig. S3a-c). In addition, some flakes with thickness of 100-200 nm instead of honeycomb-like HSC could be obtained when hydrofluoric acid was replaced with KOH to remove the ash content during the fly-silicon process (Fig. S3d). These results indicate that the fly-silicon treatment by hydrofluoric acid before KOH activation is crucial for the formation of honeycomb-like HSC.

The XRD pattern of the as-resulted honeycomb-like HSC-3 is shown in Fig. 3a. A strong and broadening peak around 24.4° can be attributed to (002) diffraction peak of turbostratic carbon, indicating the amorphous nature and low graphitization degree. The diffraction peak centered at 43° is corresponding to the (101) diffraction of graphitic carbon with amorphous or disordered nature, consistent with the HRTEM and SAED results. It is noteworthy that the intensity increases dramatically at the low-angle scattering peak indicates the presence of a large number of micropores.[38]

Fig. 3b shows the Raman spectrum of HSC-3, which can be deconvoluted into three peaks. Two characteristic peaks located around 1348 cm^{-1} (D-band) and 1590 cm^{-1} (G-band) of carbon materials can be observed. The D-band corresponds to a

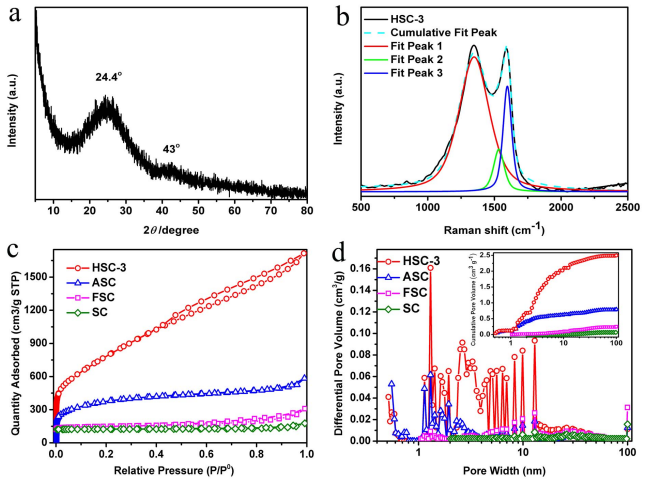

Fig. 3 (a) XRD pattern, and (b) Raman spectra of HSC-3. (c) N_2 adsorption-desorption isotherms and (d) pore size distribution calculated from the adsorption branch of the isotherm by the Nonlocal Density Functional Theory method (b) of HSC-3, ASC, FSC and SC respectively. Inset of (b) is the cumulative pore volume of HSC-3, ASC, FSC and SC.

disordered carbon or defective graphitic structure, while the G-band is attributed to in-place sp^2 C-C bond vibrations, as in planar graphite. The fired fit peak in 1530 cm^{-1} which range from 1400 cm^{-1} to 1670 cm^{-1} was assigned to amorphous graphitic phase. It is known that the I_D/I_G ratio of integrated intensities is related to the degree of structural order with respect to defects.[39] The I_D/I_G ratio of HSC-3 is about 3.7, further suggesting the structurally disordered characteristics.

Fig. 3c shows the N_2 adsorption-desorption isotherms for the as-resulted samples of HSC-3, ASC, FSC, and SC. It can be observed that the as-resulted HSC-3 exhibits a combined I/IV type adsorption-desorption isotherms with strong N_2 adsorption at relative low pressure and a development of H4 hysteresis loop over a wide relative pressure range from 0.4 to 1.0 (Fig. 3c). The strong steep increase for the N_2 uptake at low relative pressure (below 0.1) reveals the microporosity in HSC-3, while the hysteresis loop confirms the narrow slit-like mesoporous property of HSC-3. The ASC obtained from the activation of SC without fly-silicon treatment presents typical I type adsorption-desorption isotherms without obvious hysteresis loop which indicates that the ASC contains mainly micropores. The saturation in the isotherm at the higher pressure also indicated the high density of micropores in ASC.[40] It can also be seen that both FSC and SC exhibits typical IV type adsorption-desorption isotherms with H3 hysteresis loop, indicating the presence of mesopores in FSC and SC. Fig. 3d shows the pore size distribution (PSD) curves of HSC-3 and ASC calculated from the adsorption branch of the isotherms by the nonlocal density functional theory method. It can be observed that the PSD curves of HSC-3 and ASC exhibit a hierarchical pore structure that includes micro-, meso-, and macropores. It is obvious that there are little micropores in the samples of FSC and SC, which is consistence to the results of N_2 adsorption-desorption isotherms (Fig. 3d). The specific surface areas of HSC-3 and ASC were determined to be 2839

and 1272 m^2 g^{-1} (Table S2), while the pore volumes are 2.65 and 0.9 cm^3 g^{-1}, respectively. It can also be seen that both of the specific surface area and pore volume of HSC-3 are much higher than those of ASC, FSC, and SC. It is worthy of noting that the ratios of micropore-to-total-specific-surface-area and micropore-to-total-pore-volume of HSC-3 and ASC were reduced from 61.9 % to 42.9 % and 44.9 % to 25.7 %, respectively. Although the cumulative pore volume (Inset of Fig. 3d) shows that the as-resulted HSC-3 and ASC have a similar cumulative pore volume below 1.1 nm pore width, HSC-3 presents a notable growth of pore volume compared with ASC when the pore width is larger than 1.1 nm. These results indicate that the fly-silicon process before KOH activation in our work not only can remove the ash content (i.e. SiO_2), but also have significant influence on the porosity of the as-resulted HSC.

It is well known that the activation with KOH generally results in a large number of pores with sizes of less than 4 nm.[41] However, in this work, a large number of mesopores large than 4 nm in the HSC sample can be observed clearly (Fig. 3d). These results may be not only due to the high ash content of SS and unique pore structure of SC (Fig. 1c and d), but also owing to the fly-silicon treatment process by hydrofluoric acid. On the one hand, along with the removal of ash content through fly-silicon treatment, a lot of macropores existed in the SC (Fig. S2c), which are conducive to the activation process, and thus result in the improvement of mesopores in HSC. On the other hand, the larger surface area of FSC, which is three times larger than that of SC (Table S2), leads to the increase of the contact area with KOH, and thus promotes the activation efficiency and microporosity. If SC did not proceed this fly-silicon treatment, the as-resulted ASC exhibits the typical porosity of acitvated carbon with pore sizes less than 4 nm. The as-resulted ASC shows a disordered granular morphology, which is different from that of HSC (Fig. S2d). These results indicate that the introduction of fly-silicon treatment process can increase the specific surface area, change the porosity, and affect the morphology. The as-prepared HSC-3 exhibits novel 3D interconnected frameworks and hierarchically porous structures, which make it favourable for the high current density charge/discharge supercapacitors.

To evaluate the characteristics of HSC-3 as electrode materials for supercapacitors, the electrochemical capacitive performance of HSC-3 was measured by using a three-electrode system in electrolyte of 6 M KOH aqueous solution. Fig. 4a shows the CV curves of HSC-3 and ASC at a scan rate of 20 mV s^{-1}. A slightly distorted and symmetric rectangular shape can be observed from -1.0 to 0.0 V for HSC-3 and ASC, indicating the formation of an electric double layer in aqueous electrolyte and the generation of small equivalent series resistance (ESR) occurred in HSC-3 and ASC.[42] In addition, the larger area of loop in CV curve of HSC-3 than ASC suggests the higher capacitance. The triangle-like GCD curves of HSC-3 and ASC at current density of 10 A g^{-1} indicate the reversible capacitive and an ideal electric double layer capacitor (EDLC) behavior, and high charge/discharge efficiency (Fig. 4b). The resultant HSC-3 exhibits a much longer charge/discharge time

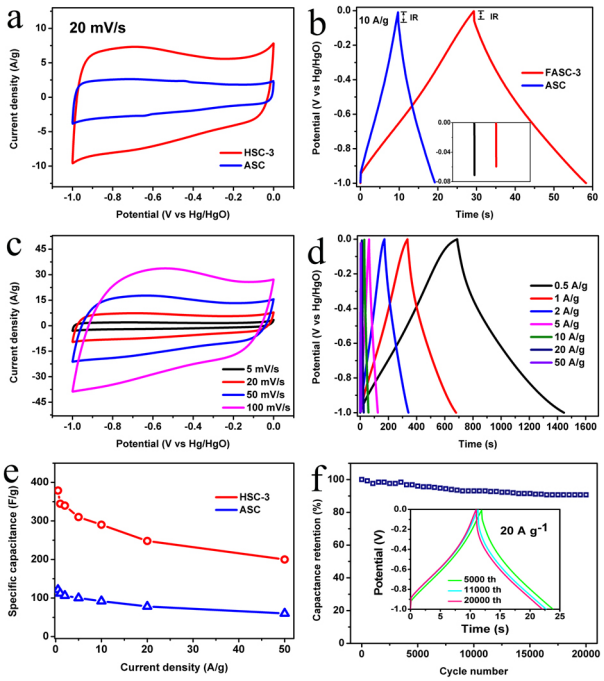

Fig. 4 (a) Cyclic voltammetry (CV) and (b) galvanostatic charge/discharge (GCD) curves of HSC-3 and ASC, respectively. Inset in (b) is the IR drops. (c) CV of HSC-3 at different scan rates. (d) GCD curves of HSC-3 at different current densities. (e) Specific capacitance of HSC-3 and ASC at different discharge densities. (f) Cyclability at a current density of 20 A g^{-1} over 20,000 cycles. Inset in (f) is GCD curves at different cycles.

than ASC, suggesting that more electrolyte ions participate in the charge/discharge process in HSC-3, and thus results to a higher specific capacitance.[43] The as-resulted HSC-3 shows a high specific capacitance of 290 F g^{-1} (1.16 F cm^{-2}) at current density of 10 A g^{-1}, which is much higher than that of ASC (95 F g^{-1} and 0.38 F cm^{-2} at 10 A g^{-1}). The larger specific capacitance may be due to the higher specific surface areas of HSC-3 (2839 m^2 g^{-1}), which is two times higher than that of ASC (1272 m^2 g^{-1}). In addition, the initial voltage loss (i.e. IR drop) observed in the discharge curves of HSC-3 is smaller than ASC at 10 A g^{-1} (as shown in Fig. 4b inset), suggesting that the as-resulted HSC-3 have faster I-V response and lower internal resistance for supercapacitors.[44] The CV curves of HSC-3 at different scan rates ranging from 5 to 100 mV s^{-1} and the GCD curves of the as-resulted HSC-3 as a function of the potential scan rates ranging varied from 0.5 to 50 A g^{-1} were also investigated. As shown in Fig. 4c, it can be seen that the CV curves show increasing current densities along with the scan rates and the quasi-rectangular CV shape of HSC-3 can be maintained superbly at higher scan rates of 100 mV s^{-1}. The rectangular degree of the CV curves could reflect the ion diffusion rate in the pores of HSC-3 electrodes.[45] The symmetric quasi-rectangular voltammograms curves of HSC-3 electrodes imply a quick ion diffusion and good charge propagation even at high scan rate. Generally, it is believed that the quick diffusion of ions in the electrode will result in an ideal rectangular shape of CV curve at high scan rate. These results indicate that the interconnected hierarchical pore structures of HSC-3 can provide a wide and short pathway for quick ion

diffusion. The specific capacitance of HSC-3 is as high as 340 F g^{-1} (1.36 F cm^{-2}) at a scan rate of 5 mV s^{-1}. The specific capacitance of HSC-3 is still retaining a high specific capacitance (258 F g^{-1} and 1.03 F cm^{-2}) even at high scan rate of 100 mV s^{-1} (Fig. S4). Fig. 4d depicts the GCD curves of HSC-3 at different current densities from 0.5 to 50 A g^{-1}. All GCD curves of the HSC-3 at various current densities are quasi-triangular and symmetrical, indicating that the electrode possesses typical EDLC behavior and superior charge/discharge reversibility. Additionally, the IR drop at the initiation of the discharge is 0.0016 V (at current density of 0.5 A g^{-1}), and enhances with the increase of the current density from 0.5 to 50 A g^{-1}. Importantly, the IR drop at an ultra high current density of 50 A g^{-1} is only 0.2 V, suggesting the excellent conductivity performance of the as-resulted HSC-3 and the lower electrochemical polarization in base aqueous media even at very high current density.[46]

The relationship between the capacitance and current density is described in Fig. 4e. A highest specific capacitance value of 379 F g^{-1} (1.52 F cm^{-2}) can be obtained at a current density of 0.5 A g^{-1}. As the current density increases, the specific capacitance decreases. In the case of a current density less than 1 A g^{-1}, the capacitance rapidly decreases with increase of the current density, whereas the capacitance decrease slowly when the current density rises from 1 A g^{-1} to 50 A g^{-1}. It can also be observed from Fig. 4e that the specific capacitance of the ASC sample decreases with the increase of the current density, which is similar to that of HSC-3. It has been known that the diffusion of active ions on the electrode surface is limited when the charging current become faster. As a result, most of micropores are not accessible to the electrolyte completely at high current density.[47] When the current increases to an ultrahigh current density of 50 A g^{-1}, the specific capacitance of HSC-3 can still be maintained to more than 200 F g^{-1} (0.8 F cm^{-2}). It is noteworthy that the capacitance retention of HSC-3 (~53 %) is higher than that of ASC (48 %), indicating an improved rate capacity of the as-resulted HSC-3 with fly-silicon treatment (Fig. 4e). The excellent capacitive performance at high current density may be due to the unique 3D interconneced hierarchical porosity of HSC-3 and abundant pores larger than 1.1 nm in size. Table S3 shows the comparison of the specific capacitance of different carbonaceous materials synthesized from biomass. It can be seen that the honeycomb-like HSC derived from high-ash-content SS in our work exhibits an excellent supercapacitive performance superior to other biomass-derived carbon materials (Table S3). These results confirm that the interconnected hierarchical porous structure of HSC is effective to improve the electrolyte accessibility and electrical conductivity, leading to fast ion response and superior rate performance.

The long-term cyclic stability of the capacitance performance of HSC-3 was investigated using GCD of 20,000 cycles at a constant current density of 20 A g^{-1}. As depicted in Fig. 4f, even after charging/discharging for 20 000 cycles at a high current density of 20 A g^{-1}, the capacitive retention is still as high as 90%, suggesting the excellent long-term electrochemical stability. The inset in Fig. 4f shows the GCD curves in different cycles, the similar quasi-triangular and symmetrical shapes indicates the typical EDLC behavior of HSC-3 was kept during the continuous charge/discharge

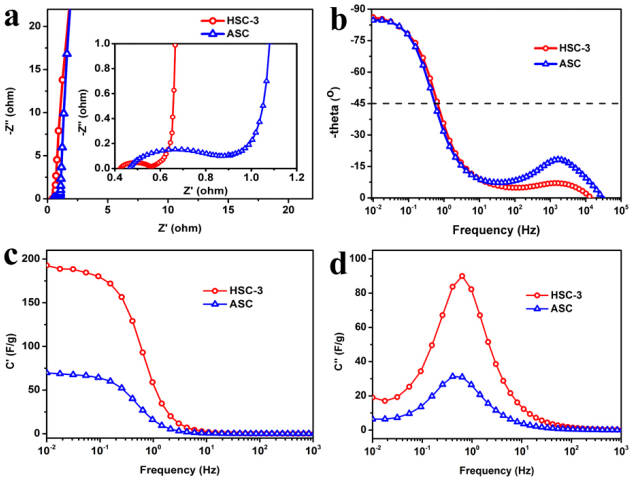

Fig. 5 (a) Nyquist plots of HSC-3 and ASC. Inset in (a) is the magnified plots in higher frequency region. (b) Bode plot of HSC-3 and ASC. C′ (c) and C′′ (d) calculated from the EIS data versus frequency for HSC-3 and ASC.

cycles. The excellent long-term cycling stability can be ascribed to the following reasons: (1) the interconnected framework of the freestanding nanosheets, which can inhibit the stack of carbon nanosheets efficiently; (2) the optimized unique hierarchical porous structure, which allows K^+ and OH^- to access to the surface with cycling and provides certain amount of adsorbent sites with reversible adsorption electrolyte easily; (3) the low resistance of HSC-3 even at high current density.

To further understand the capacitive behavior of HSC-3, electrochemical impedance spectroscopy (EIS) test was carried out over a frequency range from 100 kHz to 10 mHz. Fig. 5a shows the Nyquist plot for HSC-3 in 6 M KOH electrolyte. The approximately vertical EIS curve tails in a low frequency range indicate the nearly ideal capacitive of HSC-3 and ASC. At very high frequency, the x-intercept on the real axis (Z′) represents a combined resistance including intrinsic resistance of electrode materials, ionic resistance of electrolyte and contact resistance between electrode and current collector.[48] The x-intercept on the real axis of the HSC-3 and ASC is close, demonstrating low ESRs (0.42 and 0.46 Ohms, respectively).

The 45° line in the intermediate frequency region, called as Warburg impedance, is the characteristics of ion diffusion into the pore electrode materials. It is known that semicircles detected at high frequency can reflect the charge-transfer resistance caused by Faradic reactions and EDLC.[48] The smaller the semicircle diameter is, the lower the impedance will be. It can be seen that the honeycomb-like HSC-3 presents a smaller semicircle diameter than ASC (Fig. 5a inset). Fig. 5b shows the Bode phase plot of HSC-3 and ASC. At high frequency region, the phase angle is almost zero. A small and wide peak with decreasing frequency could also be seen. As the frequency under 100 Hz, the phase angle increases quickly with decreasing frequency and shifts to more negative values reaching -86.13° and -84.74° in the low frequency limitation region respectively, which is close to that of an ideal capacitor (-90°). The corresponding time constant τ (the inverse of the characteristic frequency at which -45° is reached in the Bode phase plots) also responded in a similar fashion, but the HSC-3 reached -45° at a slight higher frequency than ASC. The plots of frequency dependent

C′ and C″ components of the capacitance of HSC-3 and ASC are shown in Fig. 5c and d. It can be seen that the capacitance of HSC-3 at 0.01 Hz (192 F g^{-1}) is much higher than that of ASC (70 F g^{-1}), and then decreases sharply below 0.15 Hz, which is a common feature for porous carbon electrodes because the deep inner pores cannot be accessed by the electrolyte ions at high frequency, thus leads to a sharp decrease in capacitance.[49] The C″ versus frequency dependences of HSC-3 and ASC present the maxima of 0.63 Hz and 0.41 Hz, respectively (Fig. 5d). The corresponding relaxation time of HSC-3 and ASC was 1.58 and 2.43 s, respectively. The relaxation time is a quantitative measure of how fast the device can be charged/discharged reversibly and implies the minimum time needed to discharge all the energy from the device with an efficiency greater than 50%.[50] The shorter relaxation time of HSC-3 implies the faster charge/discharge reversibility and efficiency. The fast frequency response and relaxation time further confirms the superiority of the 3D honeycomb-like HSC as supercapacitor electrode for high discharge rates with good capacitance retention and high power delivery.[36,37] Nyquist plots of HSC-3 electrode before and after 20 000 repeated charge/discharge cycles show a similar x-intercept on the real axis and the similar semicircle diameter imply the excellent long-term electrochemical stability of HSC-3 electrode (Fig. S5).

The mass ratio of the activation reagent and carbon (KOH/C) is a very important factor to develop and finely adjust the pore networks in HSCs, and thus affect the electrochemical performance of HSC electrodes. Fig. S6a shows the nitrogen adsorption–desorption isotherm of HSCs obtained with different mass ratios of KOH/C. It is clear that all resulted HSC samples exhibit a combined I/IV type adsorption-desorption isotherms with H4-type hysteresis loop and a steep increase of nitrogen uptake at a low relative pressure, indicating the existence of mesopores and a considerable amount of micropores.[51] The nitrogen uptake evidently increases with increasing KOH/C ratio from 1.0 to 3.0, which indicates the improvement of porosity. Table S2 presents the porosity parameters obtained from N_2 sorption isotherm analysis. It can be observed that the specific surface area increase from 550 m^2 g^{-1} to 2839 m^2 g^{-1}, while the ratio of KOH/C raises from 1.0 to 3.0. However, a further increase of KOH/C ratio of 4.0 results in the reduction of specific surface area due to the over-activation.[52] On the other hand, the change of the KOH/C ratio will also lead to the alteration of the pore structures and size distributions. HSC-1 has the largest average pore diameter of 3.81 nm due to the incomplete activation and large average pore diameter of FSC precursor (9.67 nm). Exception for HSC-1, the average pore diameter of HSCs becomes larger as the increase of KOH/C from 2.0 to 4.0. The larger average pore diameter of HSCs as the increase of KOH/C ratios may be due to the carbon lattice expansion which was resulted from the intercalation of potassium into the carbon lattices of the matrix.[53] The PSD curves of HSC samples show the increase of pore diameter from 2.20 nm to 4.68 nm while KOH/C increase from 1.0 to 3.0 (Fig. S6b). The similar hierarchical pore structure can be seen in all HSC samples. It has been demonstrated that supercapacitors are electrochemical capacitors, which electrostatically store charges through reversible adsorption of electrolyte ions onto porous electrode materials with high surface area and pores adapted to the size of ions. Therefore, the as-resulted HSC-3 may be the promising electrode material for high-performance supercapacitors.

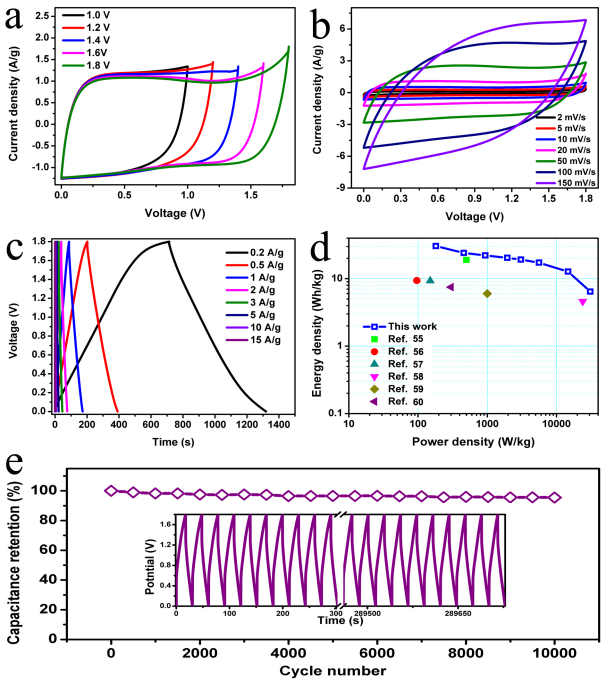

Fig. 6 CV curves of the symmetric two-electrode cell at different voltage windows in 1 M Na_2SO_4 aqueous electrolyte at scan rate of 20 mV s^{-1}, (b) CV plots of HSC-3 electrode at various scan rates, (c) GCD curves of HSC-3 electrodes at various current densities, (d) Ragone plot related to energy and power densities of HSC-3 electrode, (e) cycling stability of HSC-3 electrode after 10 000 cycles at 5 A g^{-1}.

The electrochemical properties of HSC as electrode materials for supercapacitor were also investigated. Fig. S6c shows the CV curves of HSCs electrodes at 20 mV s^{-1}. A nearly symmetric rectangular shape for the CV curve of all HSC electrodes can be kept, which implies an ideal double-layer capacitor nature of the charge/discharge process. It can be observed clearly that the as-resulted HSC-3 possesses a higher capacitance than other HSC samples from the CV curves. Fig. S6d shows typical GCD curves at a current density of 10 A g^{-1} for the HSC samples. All the charge/discharge curves were nearly linear and symmetrical. The isosceles triangular charge/discharge behavior indicates the ideal double-layer capacitive behavior. The longest discharge time of the HSC-3 means that it has the biggest specific capacitance (290.1 F g^{-1}) superior to that of HSC-1 (25.5 F g^{-1}), HSC-2 (224.1 F g^{-1}) and HSC-4 (95.2 F g^{-1}). In this work, the specific capacitance may be related to the specific surface area, that is, the enhancement of capacitance is mainly due to the relatively high specific area. These results also indicate that the optimal ratio of KOH/C for the activation of FSC is about 3, and the as-resulted honeycomb-like HSC-3 exhibits an excellent electrochemical capacitive performance superior to other HSC samples when employed as electrode materials for supercapacitors.

To explore the practical application of the as-obtained HSC for supercapacitors, an HSC-3//HSC-3 two-electrode symmetric supercapacitor was assembled with a 1 M Na_2SO_4 aqueous solution as the electrolyte. The capacitive performance of the symmetric supercapacitor with HSC-based electrodes was also investigated. Fig. 6a shows the CV curves of the symmetric

supercapacitor of HSC-3//HSC-3 operated in different voltage windows at scan rate of 20 mV s^{-1}. As expected, the rectangular shaped and nearly symmetric CV curves suggests its ideal capacitive behavior (Fig. 6a), which is well consistent with the results from the three-electrode system. It can also be seen that the supercapacitor are rectangular-like shape even at a high voltage of 1.8 V, indicating that the ideal capacitive behavior can be reversibly cycled within the voltage window of 0-1.8 V.[54] Fig. 6b displays the CV curves of the symmetric cell measured at different scan rates of 2-150 mV s^{-1} between 0 and 1.8 V. It is worth noting that CV curves still retain a relatively rectangular shape without obvious distortion with an increase in the scan rate, indicating the symmetric cell possesses excellent rate capability and ideal electrochemical capacitive behavior with rapid diffusion of electrolyte ions to the interface of the electrode. Moreover, GCD curves of the symmetric supercapacitor of HSC-3//HSC-3 were recorded at various current densities to further evaluate the electrochemical performance (Fig. 6c). The typical triangular-shape curves with low IR drop indicate the excellent electrochemical reversibility and low internal series resistance. The calculated specific capacitance based on CV and GCD curves is shown in Fig. S7. It can be seen that the capacitance is 60.7 F g^{-1} at 2 mV s^{-1} based on CV curve, and 67.8 F g^{-1} at 0.2 A g^{-1} based on GCD curves. The energy and power densities of the supercapacitor were calculated for the symmetrical supercapacitor. Fig. 6d shows the Ragone plot related to energy and power densities of HSC-3//HSC-3 symmetric supercapacitor. It is obvious that the symmetric supercapacitor exhibits the maximum energy density of 30.5 Wh kg^{-1} at a power density of 181.2 W kg^{-1} and remained 6.4 Wh kg^{-1} at a higher power density of 30 866.4 W kg^{-1}, which is higher than most of the previously reported carbon-based symmetric supercapacitors in aqueous electrolytes,[55-60] and also superior to the commercial devices (<3 Wh Kg^{-1}).[61] More importantly, the as-assembled HSC-3//HSC-3 symmetric supercapacitor exhibits capacitance retention of 95 % after 10,000 cycles (Fig. 6e), indicating the excellent long-term cycling stability.

The above results demonstrate that the as-prepared 3D honeycomb-like HCS derived from SS with high ash content is a promising electrode material for high-performance supercapacitors. The superior electrochemical performance of HSC can be attributed to the several reasons. Firstly, hierarchically interconnected honeycomb-like framework with high specific surface area provides high electronic conductivity and numerous effective electrochemical active sites to accommodate a large amount of charges. Secondly, hierarchically interconnected pores facilitate fast ion diffusion and offer unimpeded channels during rapid charge/discharge process, resulting in an enhanced charge storage and high rate capability, since sub-micrometre sized macropores can form ion buffering reservoirs, significantly shorten the ion diffusion pathways to the interior surfaces and be in favour of the electron transfer or decrease the electric resistance. Furthermore, thin carbon nanosheets with plenty of meso/micropores can provide abundant electroactive sites for the formation of electrical double layers. Finally, the interconnected freestanding nanosheets can prevent effectively the stack of HSC nanosheets, and thus leads to an ultra long-term electrochemical stability.

Conclusion

In summary, 3D hierarchical structured carbon with honeycomb-like framework and excellent electrochemical performance was prepared successfully from high-ash-content sewage sludge. The introduction of fly-silicon treatment before KOH activation results in the effective removal of the ash content, increase of specific surface area, improvement of porosity, and enhancement of electrochemical performance. The as-resulted 3D honeycomb-like HSC is suitable for high power and long life supercapacitors. The as-prepared HSC-3 exhibits high specific capacitance of 379 F g^{-1} at current density of 0.5 A g^{-1} and retains over 200 F g^{-1} at high current density of 50 A g^{-1}. Furthermore, the HSC-3 electrode shows an ultra long-term stability with capacitance retention of over 90 % after 20 000 GCD cycles at high current density of 20 A g^{-1}. The as-assembled HSC//HSC symmetric supercapacitor shows an enhanced supercapacitive behavior with a maximum energy density of 30.5 Wh kg^{-1} in aqueous solution. This work may also provide an effective way to convert other high-ash-content biomass wastes into high-valued hierarchical structured carbons, and more importantly, offer a cost-effective platform to develop advanced carbon materials for practical applications, not only in high-performance supercapacitors but also in other fields such as catalyst carriers, Li-ion batteries, gas storage, etc.

Acknowledgements

This work was supported by the National Natural Science Foundation of China (21201065, 51372091, 21371061, and 21401057), the Key Program of Science Technology Innovation Foundation of Universities (cxzd1113), the Science and Technology Plan Projects of Guangdong Province (2012B010200030), and Natural Science Foundation of Guangdong Province, China (S2013030012842, and S2012040007836).

Notes and references

H. Feng have performed most of the experiments and wrote part of the manuscript, M. Zheng and Y. Liu designed and supervised the experiments, M. Zheng also wrote most of the manuscript, H. Dong and Y. Xiao provided some helpful discussions and advices on the structure characterization of the materials, H. Hu and Z. Sun offered useful discussions on the electrochemical performance, C. Long, Y. Cai and X. Zhao carried out some electrochemical characterizations, H. Zhang and B. Lei helped preparing the manuscript.

1 A. Lag-Brotons, I. Gómez, J. Navarro-Pedreño, A. M. Mayoral and M. D. Curt, *J. Clean. Prod.*, 2014, 79, 32-40.

2 M. V. Pinna, F. Giunta, S. Nardi A. Pusino, *J. Agric. Food Chem.*, 2009, 57, 11249-11253.

3 W. Shen, Q. Guo, H. Wang, X. Yang, Y. Liu and Y. Zhang, *Environ. Eng. Sci.*, 2008, **25**, 99-105.

4 Y. Yuan, T. Yuan, D. Wang, J. Tang and S. Zhou, *Biores. Technol.*, 2013, **144**, 115-120.
5 Y. Yuan, T. Liu, P. Fu, J. Tang and S Zhou, *J. Mater. Chem. A*, 2015,**3**, 8475-8482.
6 J. M. Tarascon and D. Larcher, *Nat. Chem.*, 2015, **7**: 19-29.
7 J. B. Goodenough, *Energy Environ. Sci*., 2014, **7**, 14-18.
8 P. Simon , Y. Gogotsi and B. Dunn, *Science*, 2014, **343**, 1210-1211.
9 S. Zhang and N. Pan, *Adv. Energy mater.*, 2015, **5**, 1401401.
10 M. Beidaghi and Y. Gogotsi, *Energy Environ. Sci.*, 2014, **7**, 867-884.
11 Z. Yu, L. Tetard, L. Zhai and J. Thomas, *Energy Environ. Sci.*, 2015, **8**, 702-730.
12 J. Yan, Q. Wang, T. Wei, and Z. Fan, *Adv. Energy Mater.*, 2014, **4**, 1300816.
13 X. Li and B. Wei, *Nano Energy*, 2013, **2**, 159-173.
14 J. Chmiola, G. Yushin, Y. Gogotsi, C. Portet, P. Simon and P. L. Taberna, *Science*, 2006, **313**, 1760-1762.
15 E. Raymundo-Piñero, F. Leroux and F. Béguin, *Adv. Mater.*, 2006, **18**, 1877-1882.
16 D. Zhang, M. Miao,H. Niu and Z. Wei, *ACS Nano*, 2014, **8**, 4571-4579.
17 L. F. Chen, X. D. Zhang, H. W. Liang, M. Kong, Q. F. Guan, P. Chen, Z. Y. Wu and S. H. Yu, *ACS Nano*, 2012, **6**, 7092-7102.
18 Q. Zhao, X. Wang, J. Liu, H. Wang, Y. Zhang, J. Gao, Q. Lu and H. Zhou, *Electrochim. Acta*, 2015, **154**, 110-118.
19 V. Presser , M. Heon and Y. Gogotsi, *Adv. Funct. Mater.*, 2011, **21**, 810-833.
20 Y. Zhu, S. Murali, M.D. Stoller, K.J. Ganesh, W. Cai P.J. Ferreira, A. Pirkle, R.M. Wallace, K.A. Cychosz, M. Thommes, D. Su, E.A. Stach and R.S. Ruoff, *Science*, 2011, **332**, 1537-1541.
21 G. Sun, X. Zhang, R. Lin, J. Yang, H. Zhang and P. Chen, *Angew. Chem. Int. Ed.*, 2015, **54**, 4651-4656.
22 M. Yu, W. Wang, C. Li, T. Zhai, X. Lu and Y. Tong, *NPG Asia Mater.*, 2014, **6**, e129.
23 H. Jiang, P. S. Lee and C. Li, *Energy Environ. Sci.*, 2013, **6**, 41-53.
24 Z. Li, L. Zhang, B. S. Amirkhiz, X. Tan, Z. Xu, H. Wang, B. C. Olsen, C. M. B. Holt and D. Mitlin, *Adv. Energy Mater.*, 2012, **2**, 431-437.
25 H. Itoi, H. Nishihara, T. Kogure and T. Kyotani, *J. Am. Chem. Soc.*, 2011, **133**, 1165-1167.
26 X. Cao, Z. Yin and H. Zhang, *Energy Environ. Sci.*, 2014, **7**, 1850-1865.
27 S. B. Kulkarni, U. M. Patil, I. Shackery, J. S. Sohn, S. Lee, B. Park and S.C. Jun, *J. Mater. Chem. A*, 2014, **2**, 4989-4998.
28 D. W. Wang, F. Li, M. Liu and H. M. Cheng, *Angew. Chem. Int. Ed.*, 2008, **47**, 373-376.
29 H. F. Ju, W. L. Song and L. Z. Fan, *J. Mater. Chem. A*, 2014, **2**, 10895-10903.
30 S. Gao, K. Geng, H. Liu, X. Wei, M. Zhang, P. Wang and J. Wang, *Energy Environ. Sci.*, 2015, **8**, 221-229.
31 H. Zhu, X. Wang, F. Yang and X. Yang, *Adv. Mater.*, 2011, **23**, 2745-2748.
32 L. Wei and G. Yushin, *Nano Energy*, 2012, **1**, 552-565.
33 H. Wang, Z. Li, J. K. Tak, C. M.B. Holt, X. Tan, Z. Xu, B. S. Amirkhiz, D. Harfield, A. Anyia, T. Stephenson and D. Mitlin, *Carbon*, 2013, **57**, 318-327.
34 K. Zhou, W. Zhou, Y. Du, X. Liu, Y. Sang, W. Li, J. Lu, H. Liu and S. Chen, *Sci. Adv. Mater.*, 2015, **7**, 571-578.
35 L. Qie, W. Chen, H. Xu, X. Xiong, Y. Jiang, F. Zou, X. Hu, Y. Xin, Z. Zhang and Y. Huang, *Energy Environ. Sci.*, 2013, **6**, 2497-2504.
36 Shi K, Ren M and Zhitomirsky, *ACS Sustainable Chem. Eng*., 2014, **2**,1289–1298.
37 Shi K and Zhitomirsky I. *J. Mater. Chem. A* 2013, **1**: 11614-11622.
38 W. Qian, F. Sun, Y. Xu, L. Qiu, C. Liu, S. Wang and F. Yan, *Energ. Environ.Sci.*, 2014, **7**, 379-386.
39 C. Thomsen and S. Reich, *Phy. Rev. Lett.*, 2000, **85**, 5214.
40 Y. S. Yun, S. Y. Cho, J. Shim, B. H. Kim, S. J. Chang, S. J. Baek, Y. S. Huh, Y. Tak, Y. W. Park and S. Park, *Adv. Mater.*, 2013, **25**, 1993-1998.
41 N. P. Wickramaratne, J. Xu, M. Wang, L. Zhu, L. Dai and M. Jaroniec, *Chem. Mater.*, 2014, **26**, 2820-2828.
42 S. Kumagai, M. Sato and D. Tashima, *Electrochimica Acta*, 2013, **114**, 617-626.
43 X. Gao, W. Xing, J. Zhou, G. Wang, S. Zhuo, Z. Liu, Q. Xue and Z. Yan, *Electrochimica Acta*, 2014, **133**, 459-466.
44 K. J. Huang, J. Z. Zhang, G. W. Shi and Y. M. Liu, *Electrochimica Acta*, 2014, **132**, 397-403.
45 X. He, P. Ling, M. Yu, X. Wang, X. Zhang and M. Zheng, *Electrochimica Acta*, 2013, **105**, 635-641.
46 Q. Wang, Q. Cao, X. Wang, B. Jing, H. Kuang and L. Zhou, *J. Power Sources*, 2013, **225**, 101-107.
47 M. Biswal, A. Banerjee, M. Deo and S. Ogale, *Energ. Environ. Sci.*, 2013, **6**, 1249-1259.
48 J. G. Wang, Y. Yang, Z. H. Huang and F. Kang, *Carbon*, 2013, **61**, 190-199.
49 Z. Jin, X. Yan, Y. Yu and G. Zhao, *J. Mater. Chem. A*, 2014, **2**, 11706-11715.
50 D. Pech, M. Brunet, H. Durou, P. Huang, V. Mochalin, Y. Gogotsi, P.-L. Taberna and P. Simon, Nature nanotechnology, 2010, 5, 651-654.
51 Z. Wang, X. Zhang, X. Liu, M. Lv, K. Yang and J. Meng, *Carbon*, 2011, **49**, 161-169.
52 J. Wang, I. Senkovska, S. Kaskel and Q. Liu, *Carbon*, 2014, **75**, 372-380.
53 J. Wang and S. Kaskel, *J. Mater. Chem.*, 2012, **22**, 23710-23725.
54 X. Wu, L. Jiang, C. Long and Z. Fan, *Nano Energy*, 2015, **13**, 527-536.
55 P. Hao, Z. Zhao, J. Tian, H. Li, Y. Sang, G. Yu, H. Cai, H. Liu, C. Wong and A. Umar, *Nanoscale*, 2014, **6**, 12120-12129.
56 Q. Liang, L. Ye, Z.-H. Huang, Q. Xu, Y. Bai, F. Kang and Q.-H. Yang, *Nanoscale*, 2014, **6**, 13831-13837.
57 Z. Ling, G. Wang, M. Zhang, X. Fan, C. Yu, J. Yang, N. Xiao and J. Qiu, *Nanoscale*, 2015, **7**, 5120-5125.
58 A. B. Fuertes and M. Sevilla, *ChemSusChem*, 2015, **8**, 1049-1057.
59 L. F. Chen, Z. H. Huang, H. W. Liang, H. L. Gao and S. H. Yu, *Adv. Funct. Mater.*, 2014, **24**, 5104-5111.
60 F. Gao, G. Shao, J. Qu, S. Lv, Y. Li and M. Wu, *Electrochimica Acta*, 2015, **155**, 201-208.
61 Y. Gogotsi and P. Simon, *Science*, 2011, **334**, 917-918.